Nano Energy 38 (2017) 350–357

Contents lists available at ScienceDirect

Nano Energy

journal homepage: www.elsevier.com/locate/nanoen

Full paper

Superior reversible tin phosphide-carbon spheres for sodium ion battery anode

Xiulin Fan[a], Tao Gao[a], Chao Luo[a], Fei Wang[a], Junkai Hu[b], Chunsheng Wang[a,*]

[a] Department of Chemical and Biomolecular Engineering, University of Maryland, College Park, MD 20742, USA
[b] Department of Chemistry & Biochemistry, University of Maryland, College Park, MD 20742, USA

ARTICLE INFO

Keywords:
Sodium ion batteries
Anodes
Coulombic efficiency
Tin phosphide

ABSTRACT

Sodium ion batteries (SIB) have potential for large scale renewable energy storage due to geopolitical abundance of Na. However, the high capacity Na-ion anodes still suffer from poor cycling stability and low Coulombic efficiency (CE). Herein, uniform Sn_4P_3@C spheres were synthesized by a facile aerosol spray-pyrolysis-phosphidation method. By tuning the electrolyte, a reversible capacity of ~ 800 mAh/g with an extremely low capacity decay rate of 0.09% per cycle was achieved with a record-high initial CE (> 90%) and high cyclic CE (~ 99.9%). The Sn_4P_3@C in the stable ether-based electrolyte shows the highest accumulated cycling capacities in the reported SIB anodes.

1. Introduction

The challenges for sodium ion batteries (SIB) are the low energy density and short cycle life. Extensive efforts have been devoted to explore high capacity and long cycling cathode and anode materials for SIBs [1–5]. For the anodes, the alloying materials such as phosphorus- and Sn-based materials [6–13] have very high gravimetric capacities and volumetric capacities and proper charge/discharge potentials, which are ideal for SIB anodes. However, high capacities generate large volume changes, which pulverize the anode material and result in SEI breaking/reforming during charge/discharge cycles. The SEI breaking/reforming reduces Coulombic efficiency (CE) during cycling and consume the electrolyte and Li-ion source from cathode, resulting in poor cycling life of Na-ion full cells [14].

Nanostructured materials have been adopted to reduce the pulverization of alloy anodes, thus successfully extending the cycle life of anode materials [15,16]. However reducing the anode materials into nanoscale increases surface area between electrode and electrolyte, lowering the CE in the first several charge/discharge cycles. Although adding SEI-stabilizing FEC additives into the electrolyte can enhance cycling stability by forming a thick and dense SEI [14], it also further reduces the initial CE. P/Carbon nanotube anodes only show a low initial CE of 69% in FEC-added carbonate electrolyte [6], although a high reversible capacity of > 700 mAh/g was achieved in 30 cycles. We significantly extended the cycling life of P/Carbon nanotube anode to 2000 cycles using the vaporization-condensation synthesis method [11]. However, the initial CE is still very low (~ 68%). Alloying P with Sn to form Sn_4P_3 compounds can slightly increase the initial CE to 75–77% in FEC-added electrolytes [7,10]. The cycling life of Sn_4P_3/C can be largely extended by reducing the particle size to nanoscale. However, the initial CE of Sn_4P_3/C nano-composites were significantly reduced to 40–50% [17,18]. It is very challenging to achieve both the long cycle life and high CE for high capacity anodes.

To accomplish a long cycling performance and a high CE, the ideal anode materials should have micro-sized primary particles consisting of nano-sized secondary high capacity active materials and nanopores in a carbon matrix, so that SEI only forms on the primary particle surface, while the electronic conductive nanoporous composite can well maintain integration during charge/discharge cycles. Herein, we report such a high capacity anode, pomegranate-structured Sn_4P_3@C spheres, which were synthesized by a facile method of aerosol spray-pyrolysis and subsequent low temperature phosphidation. We demonstrated that such Sn_4P_3@C spheres could deliver a highly reversible capacity of > 700 mAh/g with record-high initial CE of ~ 90% and cycling CE of ~ 99.9% in the ether-based electrolyte, achieving both long cycle life and high CE. The pomegranate-structured Sn_4P_3@C spheres show the highest "accumulated capacities" in all reported Na-ion anodes. The accumulated capacities at Nth cycles (N is the cycle number) was defined and calculated by multiplying the capacity at Nth cycles with all the CEs before Nth cycles, which is utilized to convert the capacity of anode tested in half-cell to the true anode capacity in a full cell.

* Corresponding author.
E-mail address: cswang@umd.edu (C. Wang).

http://dx.doi.org/10.1016/j.nanoen.2017.06.014
Received 13 March 2017; Received in revised form 6 June 2017; Accepted 6 June 2017
Available online 08 June 2017

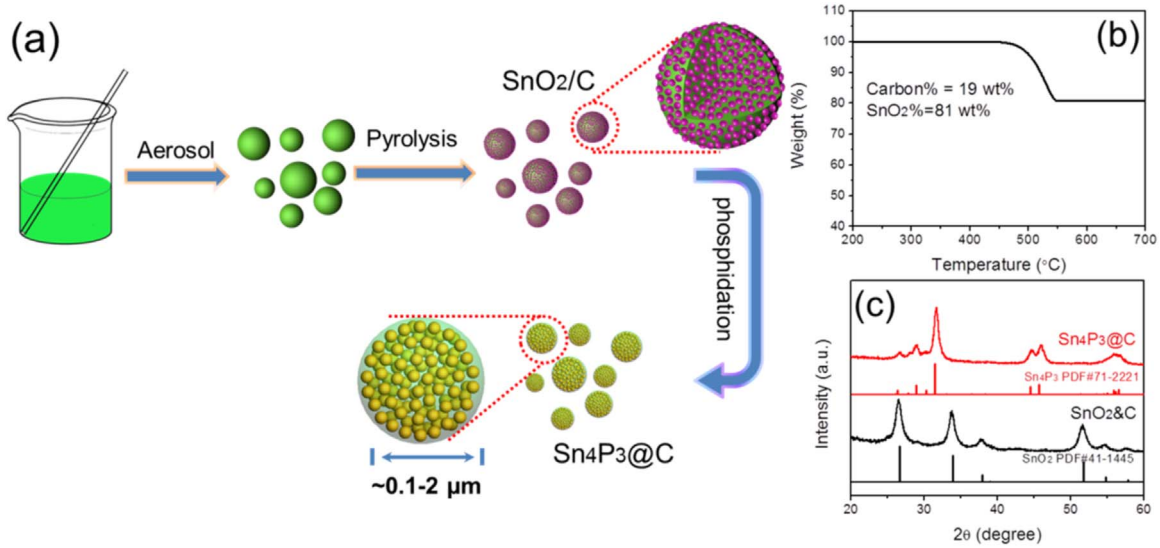

Fig. 1. (a) Schematic illustration of the fabrication process for Sn_4P_3@C pomegranates. (b) TGA results of SnO_2/C sphere template synthesized by aerosol-pyrolysis. (c) XRD patterns for the SnO_2/C sphere template and the Sn_4P_3@C pomegranates.

2. Synthesis of pomegranate-structured Sn_4P_3@C spheres

Fig. 1a illustrates the detailed synthesis process for the pomegranate-structured Sn_4P_3@C spheres. First, monodisperse well-defined SnO_2/C microspheres were facilely fabricated by aerosol-spray-pyrolysis method in the presence of sucrose and sulfuric acid in water-ethanol solution (Scheme S1). Then, these SnO_2/C microspheres were hand milled with NaH_2PO_2 and heated at 280 °C for 10 min, during which SnO_2 nanoparticles were reduced and in situ chemically transformed into Sn_4P_3 nanoparticles, resulting in uniform Sn_4P_3@C spheres. The amorphous carbon content in the SnO_2/C template is about 19 wt% as measured by TGA analysis (Fig. 1b). The X-ray diffraction (XRD) pattern in Fig. 1c identified the tetragonal phase of SnO_2 (JCPDS No. 41-1445) after aerosol-pyrolysis. As shown in SEM, TEM and HRTEM in Fig. S1, these template SnO_2/C particles are ideal spheres with a diameter of 0.1–2 μm, which consists of thousands of secondary SnO_2 nanoparticles with size of ~ 5 nm.

After low-temperature phosphidation, the SnO_2 nanoparticles transform to Sn_4P_3 with a rhombohedral structure (JCPDS No. 71-2221, Fig. 1c). The spherical structure was well inherited for the Sn_4P_3@C composite (Fig. 2a). Different from the uniform dispersion of SnO_2 in the carbon matrix with a number of nanoparticles protruding out of the surface of the carbon spheres (Fig. S1), almost all of the as-formed Sn_4P_3 nanoparticles are well encapsulated by the carbon layer, as shown in Fig. 2b, c, d, and e. The secondary particle size of Sn_4P_3 is about 20–40 nm (Fig. 2b and d), which is larger than that of SnO_2 (5 nm). Some voids are in situ formed (Fig. 2d) due to the merging of some Sn_4P_3 nanoparticles during reduction of SnO_2 in the phosphidation processes. Fig. S2 depicts the N_2 adsorption/desorption isotherms and the corresponding pore size distribution determined by the Barrett-Joyner-Halenda (BJH) model for the aerosol-spray-pyrolysis-phosphidation Sn_4P_3@C and ball milled Sn_4P_3/C composite. The pore size distribution shows that the Sn_4P_3@C exhibits a mixed meso-/macroporous structure. These internal pores should mitigate the fracture of the secondary particles during sodiation and desodiation. The observed lattice spacing of about 0.28 nm in Fig. 2f corresponds to the (107) plane distance of rhombohedral Sn_4P_3. The SEM image (Fig. 2g) and corresponding element mappings (Fig. 2h, i and j) reveal that Sn and P elements are overlapped, confirming the Sn_4P_3 nanocrystallites are well dispersed in the spheres. The tin and phosphorus atomic ratio in these spheres is about 58:42 based on the EDS spectra, in good agreement with the stoichiometric ratio of Sn_4P_3. Such a result is also highly consistent with the XRD measurement (Fig. 1c), which clearly shows the pure phase of Sn_4P_3. The carbon content in the Sn_4P_3@C spheres is about 24 wt%, as measured by weighting the residual carbon after completely etching the Sn_4P_3 species, which is slightly higher than carbon content (19%) in parent SnO_2/C spheres (Fig. 1b). In summary, the primary Sn_4P_3@C spheres bears close resemblance to the hierarchy of a pomegranate, where the secondary Sn_4P_3 nanoparticles are embedded in the matrix of carbon. The hierarchical pomegranate-structure has multiple advantages [19,20]: i) the nanosized secondary Sn_4P_3 active materials, void space and the carbon layer should effectively prevent the pulverization of Sn_4P_3 and fracture of the primary Sn_4P_3@C spheres; ii) carbon matrix and coating layer functions as an electrical conductor and a mechanical backbone so that all Sn_4P_3 nanoparticles are electrochemically active. All of these features should ensure a good electrochemical cycling performance for Sn_4P_3@C anode.

3. Electrochemical performance of Sn_4P_3@C spheres

CE is one of the most important parameters for the high capacity anodes (Fig. S3). We evaluated electrochemical reduction stability of several electrolytes with different solvents (Fig. S4) from 1.5 V to 0.0 V vs. Na/Na^+. A broad reduction peak in a wide potential range of 0.0–1.5 V was observed in $NaPF_6$-EC/DMC electrolyte and a large peak at 0.4 V appears in $NaPF_6$-EC/DMC+10%FEC. However, no obvious peaks were detected in the electrolyte of $NaPF_6$-DME and the reaction current is less than half of values in carbonate electrolytes, which demonstrated that $NaPF_6$-DME is much stable at a low potential, thus can significantly increase the initial CE. The small and quickly reduced current with charge/discharge cycles in $NaPF_6$-DME electrolyte should be attributed to minor reduction of electrolyte and impurity in the electrolyte (Fig. S4c and S4d). Fig. 3a shows the first cycle charge/discharge curves for the Sn_4P_3@C electrode using three different electrolytes at a current of 50 mA/g. The obvious plateau in the discharge at 1.2 V in $LiPF_6$-EC/DMC+10%FEC electrolyte with a lowest CE of 59.8% could be attributed to the decomposition of FEC forming dense SEI layers, which is consistent with the electrochemical stability test (Fig. S4b) and previous reports [18]. Removing the FEC from the carbonate electrolyte, the first CE increases to 72.7%, but still much lower than that in DME electrolyte. A significantly high initial CE of 90.7% is observed for the Sn_4P_3@C in DME electrolyte, demonstrating one of the highest CE in all Sn and P compounds reported to date [9,10,18]. The small amount of irreversible capacity is possibly due to the impurities in the electrolyte and the formation of thin SEI layer.

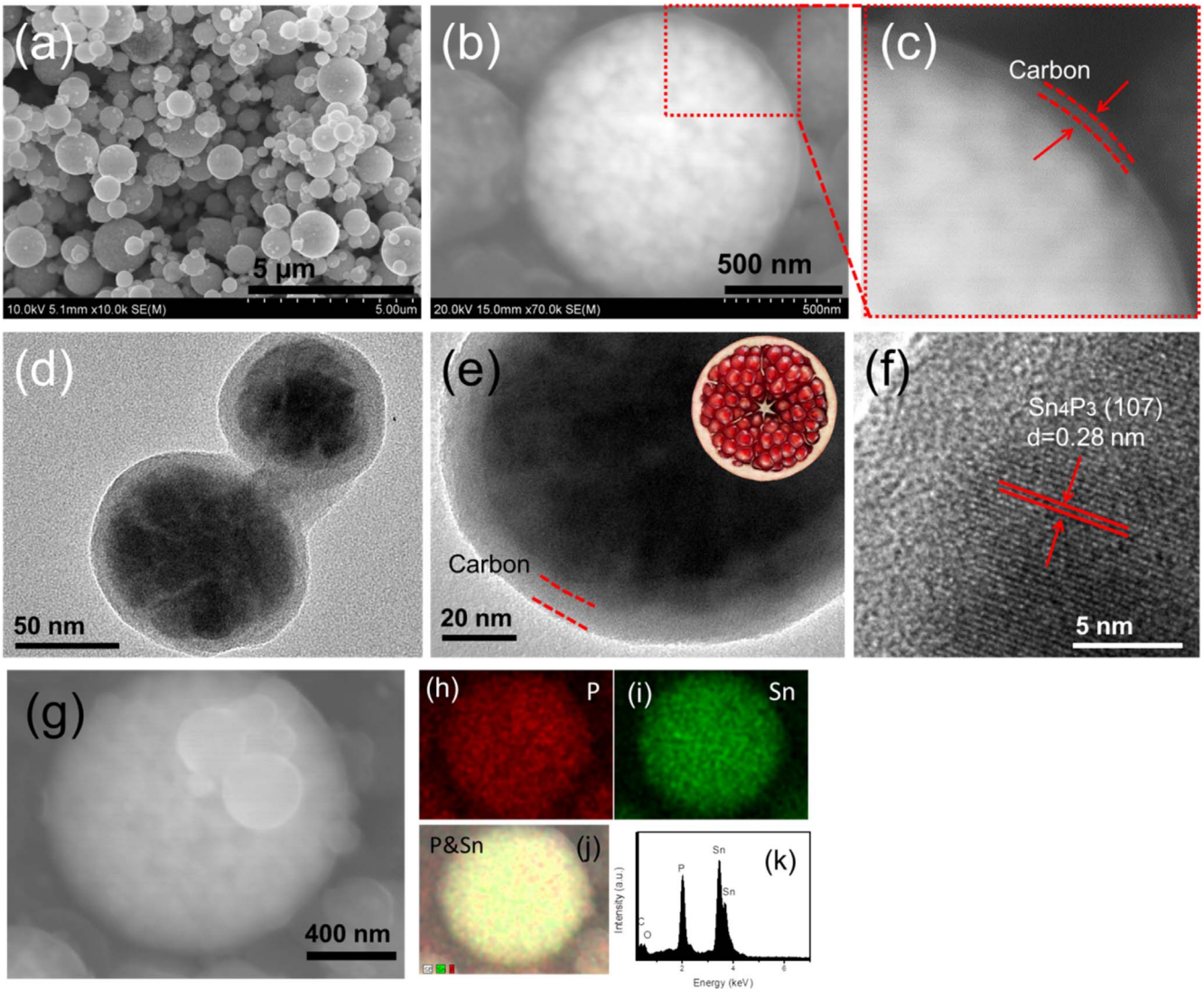

Fig. 2. SEM (a-c), TEM (d, e), and HRTEM (f) images of the as-synthesized pomegranate-structured Sn_4P_3@C spheres. (g), (h), (i), (j) and (k) shows SEM image and the corresponding EDS elemental mapping of P, Sn, overlap of these two elements and the overall EDS spectra for the Sn_4P_3@C spheres. The inset of (e) shows the ideal pomegranate structure.

The galvanostatic discharge/charge profiles of different cycles for Sn_4P_3@C in $NaPF_6$-DME electrolyte are shown in Fig. 3b. The discharge voltage profiles of Sn_4P_3@C show two plateaus located at ~ 0.25 V and 0.01 V vs. Na^+/Na, which is well consistent with the previous work, and could be attributed to the formation of Na_xP and Na_ySn [10,18]. The sodiation and desodiation reactions follow the subsequent equations:

In the initial sodiation step:

$$Sn_4P_3 + 24Na^+ + 24e^- \rightarrow Na_{15}Sn_4 + 3Na_3P \quad (1)$$

The subsequent charging/discharging cycles can be characterized by reversibly alloying and de-alloying Na_3P and $Na_{15}Sn_4$ [9,10,18]:

$$Na_{15}Sn_4 \leftrightarrow 4Sn + 15Na^+ + 15e^- \quad (2)$$

$$Na^3P \leftrightarrow P + 3Na^+ + 3e^- \quad (3)$$

As shown in Fig. 3c, the Sn_4P_3@C anode in $NaPF_6$-EC/DMC shows fast capacity decay from 700 mAh/g in the third cycle to 380 mAh/g after 110 cycles. Yet, it is still much stable compared to the previously reported tin phosphide composites [9,10], which may be due to unique pomegranate-structure of Sn_4P_3@C spheres. As the FEC was added into the electrolyte, much better cycling performance was observed. A reversible capacity of 580 mAh/g can be obtained after 120 cycles, with a capacity retention of 95% from the 2nd to 120th cycle. This indicates that thick SEI layers formed from reduction of the FEC additive can prevent the continuous side reactions of the electrolyte and the electrode [21], resulting in better cycling performance. As the electrolyte changes to $NaPF_6$-DME, the cycling stability is similar to the EC/DMC + 10%FEC system, but shows a much higher reversible capacity. After 120 cycles, the Sn_4P_3@C anode in $NaPF_6$-DME electrolyte still delivers a reversible capacity of over 700 mAh g^{-1}, which is one of the highest specific capacities for Sn-based anode materials. The mechanism for the high capacity in $NaPF_6$-DME electrolyte was investigated using electrochemical impedance spectroscopy (EIS). The semicircles at the high frequency range in EIS (Fig. 3d) represent the total interfacial resistance from SEI and the charge transfer resistance. The Sn_4P_3@C in DME electrolyte has a lowest interfacial resistance of ~ 250 Ω (vs. ~ 750 Ω for EC/DMC + 10% FEC). This phenomenon illustrates that much better electrode stability and more favorable sodiation/desodiation kinetics can be achieved for pomegranate-structured Sn_4P_3@C in DME electrolyte, which is confirmed by the much better rate capability for the Sn_4P_3@C in $NaPF_6$-DME electrolyte (Fig. S5). The electrochemical performance of ball milled Sn_4P_3/C composite was also evaluated. As shown in Fig. S6, the capacity of the ball milled Sn_4P_3/C composite decays very fast in the 1 M $NaPF_6$ DME electrolyte, demonstrating that the pomegranate structure plays a significant role in stabilizing the cycling performance.

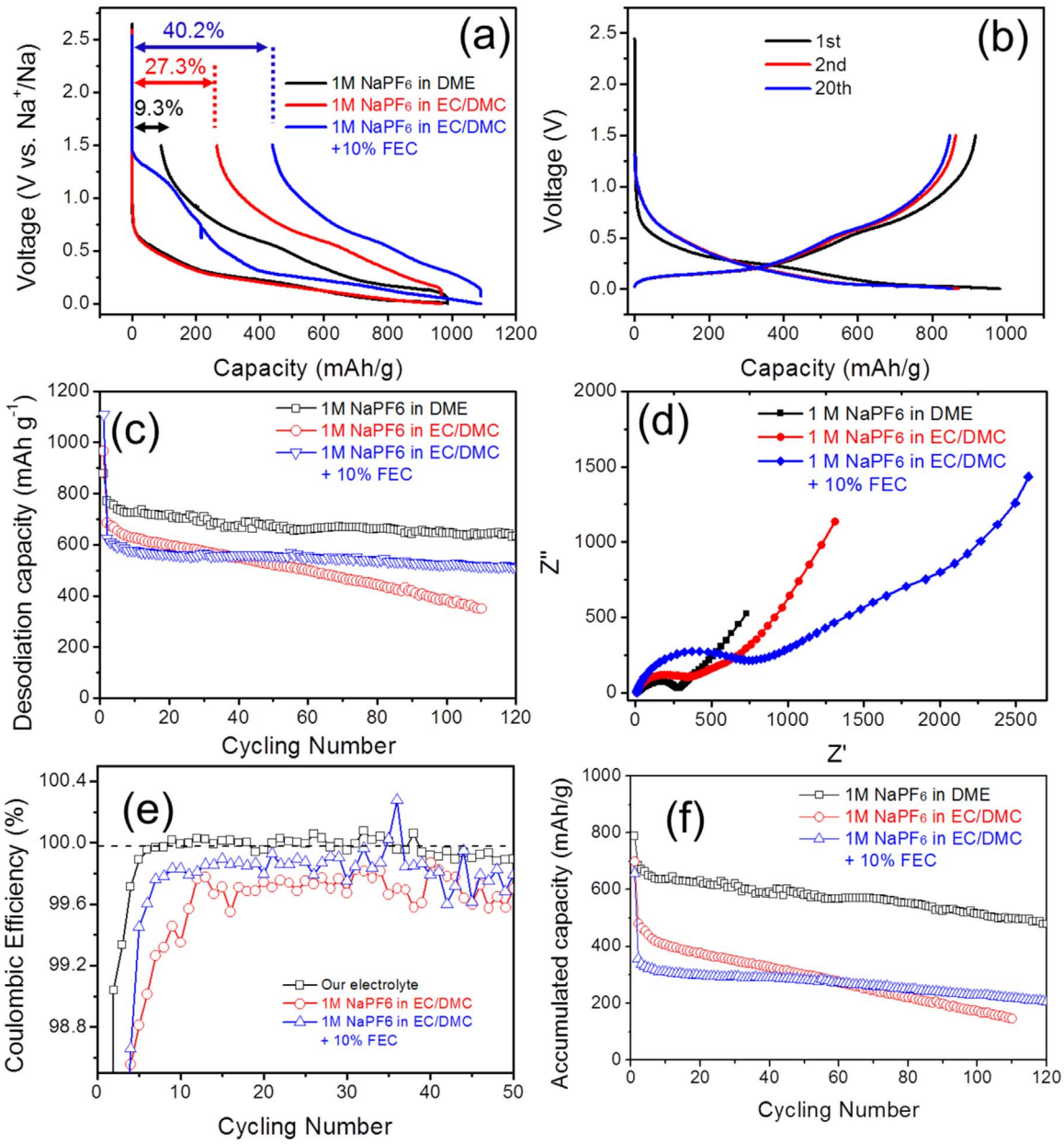

Fig. 3. Electrochemical performance of pomegranate-structured Sn_4P_3@C composite. (a) Initial galvanostatic charge-discharge voltage profiles of composite at a current density of 50 mA/g using three different electrolytes. (b) Galvanostatic charge-discharge voltage profiles of pomegranate-structured Sn_4P_3@C composite at a current density of 50 mA/g using 1 M $NaPF_6$ in DME as the electrolyte. (c) cycling performances of pomegranate-structured Sn_4P_3@C nanospheres at the 100 mA/g using different electrolytes. (d) Nyquist plots for Sn_4P_3@C composite cycled in three different electrolytes after 10 cycles. (e) Coulombic efficiency for the pomegranate-structured Sn_4P_3@C composite cycled in three different electrolytes. (f) accumulated cycling performance for the pomegranate-structured Sn_4P_3@C composite cycled in three different electrolytes considered the Coulombic efficiency.

Fig. 3e shows the cyclic CE of the Sn_4P_3@C in these three electrolytes at the 100 mA/g. For EC/DMC and EC/DMC-10%FEC electrolytes, the Sn_4P_3@C electrode possesses a CE of 99.6% and 99.8% after about 10 charge/discharge cycles, respectively. The CE of Sn_4P_3@C quickly increases to 99.9% after 6 cycles in relatively stable $NaPF_6$-DME electrolyte, which is the highest cyclic CE ever reported for alloying anode materials for SIBs (Table S1). The high CE for Sn_4P_3@C in DME electrolyte is consistent with the electrochemical stability tests (Fig. S3) and small interfacial resistance (Fig. 3d). The thin and spatially confined SEI on Sn_4P_3@C in DME electrolyte highly increases the CE.

The morphology and elemental distribution on Sn_4P_3@C spheres after charging/discharging in three electrolytes for 10 cycles was directly characterized using SEM, TEM and XPS, shown in Fig. 4 and Fig. S7. All of the spherical structures are well preserved for these samples cycled in the three different electrolytes (Fig. 4a, f, and j), indicating that the pomegranate architecture ideally accommodate the volume expansion during sodiation as we expected. For the Sn_4P_3@C cycled in EC/DMC + 10% FEC, a thick and relatively dense layer mainly containing Na and F were observed (Fig. 4d, e, k, l and m). No any primary Sn- or P-containing particles can be observed. The red dash arc in Fig. 4e shows that the Na concentrated in the out layer of the sphere. As for Sn_4P_3@C cycled in EC/DMC, porous layer on the surface of the spheres were detected, the red arrows in Fig. 4j illustrate the pores in the SEI layer. The uniform distribution of Na (Fig. 4f, and i) indicates the SEI layer in 1 M $NaPF_6$-DME electrolyte is much thinner than that cycled in carbonate electrolytes. The primary Sn- or P-containing nanoparticles can still be observed in the spheres encapsulated by the thin carbon layer (Fig. 4f). XPS shows that small amount of NaF can be observed on the surface of Sn_4P_3@C in DME

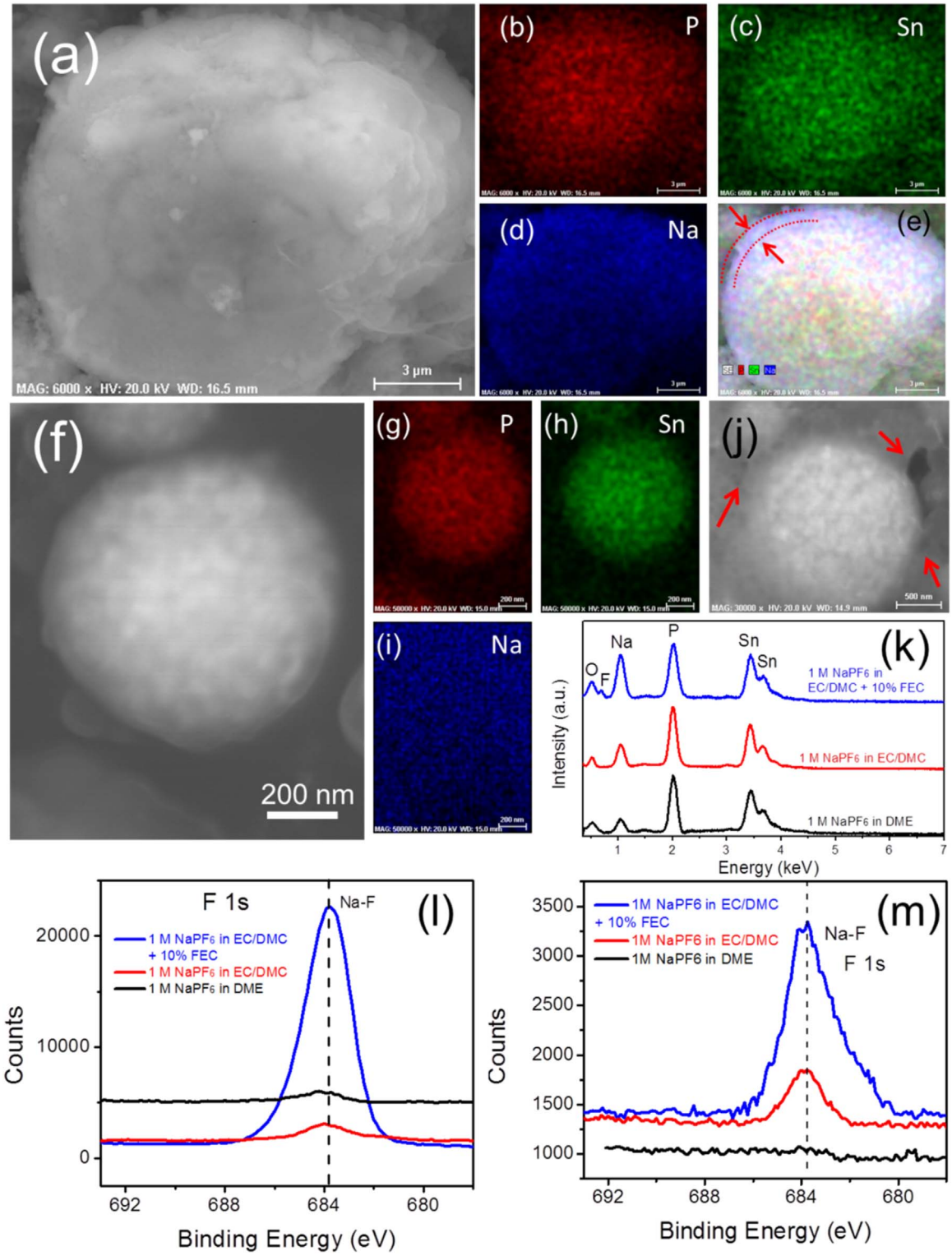

Fig. 4. SEM images, corresponding EDS elemental mapping and XPS characterizaiton of pomegranate-structured Sn_4P_3@C anode after 10th cycle (desodiation state) in different electrolytes. SEM image and EDS mapping of Sn_4P_3@C: (a, b, c, d, and e); 1 M $NaPF_6$ in EC/DMC + 10 mol% FEC (f, g, h, and i) 1 M $NaPF_6$ in DME; (j) 1 M $NaPF_6$ in EC/DMC; (k) the overall EDS spectra in these three electrolytes. XPS characterization of F 1s peak for the pomegranate-structured Sn_4P_3@C anode after ten cycles in different electrolytes: (l) after washing with DMC three times without sputtering; (m) after 20 min of Ar sputtering.

electrolyte, which is formed by reduction of the electrolyte on the Sn_4P_3@C surface (Fig. 4l and m). Formation of much thinner SEI on Sn_4P_3@C in DME solvent electrolyte than that in EC/DMC and EC/DMC + 10% FEC electrolytes was also confirmed by C 1s signals before and after sputtering (Fig. S7).

Due to excess of electrolytes and Na source of Na metal in Na/Sn_4P_3@C half-cell, cycling stability of Na/Sn_4P_3@C in half cells cannot reveal the stability of full cells (Fig. S3). The consequent implication of the low CE is that these anodes can only be assembled into a cell with a much excess of the cathode materials to offset the every cycle's depletion of the ions, which will dramatically lead to a lower energy density for the full cell and therefore is not practical for the SIB

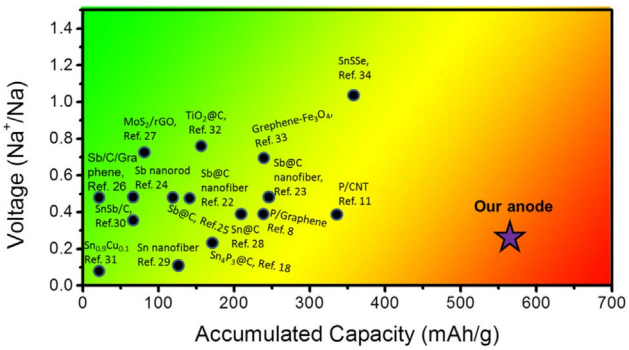

Fig. 5. Accumulated capacity for our pomegranate-structured Sn_4P_3@C material in 1 M $NaPF_6$-DME electrolyte after 100 cycles and compared with some published SIB anodes. The accumulated capacities for the published SIB anodes are calculated based on the initial reversible capacity and the average cyclic CE assuming that there is no capacity decay due to active materials peeling off from the current collector and all of anode materials are electrochemical active during cycling.

industry. Hence, meaningful capacity of an electrode at Nth (N is the cycle number) cycles should be calculated by multiplying the electrode capacity at Nth cycles with all CEs before Nth cycle. We define this meaningful capacity as an "accumulated capacities", which reflects the anode capacity in a full cell. Here, we compared the Sn_4P_3@C electrode cycled in three different electrolytes based on the "accumulated capacities" (as shown in Fig. 3f), which is calculated based on the following equation:

$$\text{Capacity}_{\text{Nthcycle}}(\text{accumulated})=\text{Capacity}_{\text{Nthcycle}}(\text{halfcell}) \times [CE_1 \times CE_2 \times CE_3 \times CE_4 \ldots \times CE_n] \quad (4)$$

For the Sn_4P_3@C cycled in $NaPF_6$-DME, an accumulated capacity of over 570 mAh/g can be obtained after 120 cycles, which is more than two and three times higher than cycled in EC/DMC-10% FEC (230 mAh/g) and in EC/DMC (148 mAh/g), respectively. The Sn_4P_3@C in relatively stable $NaPF_6$-DME electrolyte shows the highest accumulated capacity in all anodes ever reported (Fig. 5) for SIBs [8,11,18,22–34].

A full cell using pomegranate-structured Sn_4P_3@C spheres as anode, $Na_3V_2(PO_4)_3$ (denoted as NVP, Fig. S8) as cathode [35], was evaluated in $NaPF_6$-DME electrolyte. NVP can provide 90 mAh/g (Fig. S9) in Na/NVP half cell. Sn_4P_3@C/NVP full cell was assembled with a mass ratio of NVP to Sn_4P_3@C of 9 to balance the capacity between two electrodes. The full cell shows an initial charge capacity of 100 mAh/g and a discharge capacity of 79 mAh/g at a rate of C/5 with stable cycling capacity (Fig. S10). The irreversible capacity loss is mainly due to the side reactions between the electrolyte and the as-synthesized NVP [35], as shown in NVP/Na half-cell (Fig. S9). In the test cycles, the Sn_4P_3@C/NVP full cell delivers an energy density over 210 Wh/kg taking account the mass of the active materials in both the cathode and anode sides. The full cell demonstrates that our Sn_4P_3@C anode associated with the DME electrolyte can be facilely paired with the current cathode materials of SIBs. Further improvements on the energy density of the full cell should be achieved on both optimization of cathode materials and balancing the ratio of the cathode to anode.

In conclusion, we have synthesized pomegranate-structured Sn_4P_3@C spheres by a facile aerosol spray-pyrolysis-phosphidation method, in which Sn_4P_3 nanoparticles with size of 20–40 nm are encapsulated by the thin carbon layers. Benefiting from the rationally designed pomegranate-architectured spheres and the stable ether electrolyte, a high reversible capacity over 700 mAh/g with high CE (initial CE > 90%, cyclic CE ~ 99.9%) was obtained for over 120 cycles. The capacity at Nth (N is the cycle number) cycles obtained in Na/Sn_4P_3@C half-cell with excess electrolyte was converted as accumulated capacity by multiplying the electrode capacity at Nth cycles with all CEs before Nth cycle to reflect the true capacity in full cell. Sn_4P_3@C spheres delivers the highest accumulated capacity in the reported anode materials for SIBs. Such outstanding performance of this anode with high reversibility and high CE will pave the way for practical applications of alloying anodes in commercialization of SIBs.

4. Methods

4.1. Synthesis of SnO_2/C nanospheres

The template of SnO_2/C nanospheres were synthesized by a facile and low-cost aerosol-spray pyrolysis route. In a typical synthesis process, $SnSO_4$ (3 g), sucrose (1 g) and sulfuric acid (2 mL, 98%) were dissolved into a 100 mL mixture of ethanol and distilled water (1:1). The solution was atomized by Ar flow with a collision-type nebulizer (Atomizer Aerosol Generator ATM 220, TOPAS, Germany), and the aerosols that were generated subsequently entered a tubular furnace at 600 °C. The flow rate of the precursor solution vapor was about 200 $cm^3\ s^{-1}$. During the pyrolysis, $SnSO_4$ was in situ decomposed to SnO_2 nanoparticles and the sucrose transformed to carbon at the catalysis of sulfuric acid.

4.2. Synthesis of pomegranate-structured Sn_4P_3@C nanospheres

To prepare pomegranate-structured Sn_4P_3@C nanospheres, the as-synthesized SnO_2/C spheres were hand milled with NaH_2PO_2. The molar ratio of Sn to P was 1:5. Subsequently, the mixture was heated at 280 °C for 5 min with a heating rate of 10 °C min^{-1}. After cooling down, Sn_4P_3@C spheres were collected by washing the mixtures with diluted HCl aqueous solution (0.05 mol/L), water and ethanol, respectively.

4.3. Synthesis of Sn_4P_3/C composite

The Sn_4P_3/C composite were prepared by ball milling under an argon atmosphere. The active materials (Sn and P): carbon black weight ratio was set to 76:24. The Sn:P ratio was 4:3 by molar ratio. The weight ratio of milling balls to powder was 40:1. The rotation speed of the mill was set to 400 rpm for 24 h.

4.4. Materials characterization

The crystalline structure of the materials was characterized by powder X-ray diffraction (XRD) on a Bruker Smart1000 diffractometer with a Cu Kα radiation. The morphology and microstructure of the sample was investigated by scanning electron microscopy (SEM, Hitachi SU-70) and transmission electron microscopy (TEM, JEM 2100 LaB_6, 200 keV). X-ray photoelectron spectroscopy (XPS) was conducted on a high sensitivity Kratos AXIS 165 X-ray photoelectron spectrometer with Mg K_α radiation. All binding energy values were referenced to the C 1s peak of carbon at 284.6 eV. Before the XPS characterizations, the cycled electrodes were washed with the corresponding solvents (DME for the 1 M $NaPF_6$-DME electrolyte, and DMC for 1 M $NaPF_6$-EC/DMC electrolyte and 1 M $NaPF_6$-EC/DMC + FEC electrolyte) for several times to remove the salts. Thermogravimetric analysis was carried out using a TA Q600 (USA) in air at a heating rate of 5 °C min^{-1}. Pore size distributions, specific surface areas and pore volumes of the samples were characterized by N_2 adsorption by means of a Micromeritics ASAP 2020 Porosimeter Test Station. Samples were degassed (in a vacuum) at 180 °C for 12 h before the test. The specific surface areas were calculated using the Brunauer-Emmett-Teller (BET) method from the adsorption branch. The porosity distribution was calculated from adsorption branch using the BJH (Barrett–Joyner–Halenda) equation.

4.5. Electrochemical measurements

Electrolytes are prepared by adding $NaPF_6$ into various anhydrous solvents (DME, EC/DMC, EC/DMC + 10%FEC). All the solvents were dried by molecular sieve (4 Å, Sigma-Aldrich) to make sure the water content to be lower than 10 ppm, which is tested by Karl-Fisher titrator (Metrohm 899 Coulometer). The charge-discharge performances of the electrode materials were examined by 2032 type coin cells. The Sn_4P_3@C composite with carbon black and sodium alginate dissolved in water were mixed at a weight ratio of 70:15:15 to form a slurry, which was then pasted on the Cu foil and dried to obtain working electrodes. Pure Na foil was used as counter and reference electrode. The electrochemical performance of pomegranate-structured Sn_4P_3@C spheres for the Na^+ ion insertion/de-insertion was investigated in different electrolytes. A three-electrode "T-cell" was utilized to test the stability window of the different electrolytes with a polished stainless steel as the working electrode, Na foils as the reference and counter electrodes. Cyclic voltammetry (CV) testing with voltages ranging from 0 to 1.5 V under a scan rate of 10 mV/s was recorded using a Gamry 1000E electrochemical workstation (Gamry Instruments, USA). All the cells were assembled in a glove box with water/oxygen content lower than 2 ppm and tested at room temperature. The galvanostatic charge/discharge test was conducted on Arbin battery test station (BT2000, Arbin Instruments, USA). $Na_3V_2(PO_4)_3$ (NVP) was used as cathode in a full cell to couple with our pomegranate-structured Sn_4P_3@C composite. A conventional solid-state reaction was used to prepare NVP according to the previously reported protocol.

Acknowledgements

This work was supported as part of the Nanostructures for Electrical Energy Storage (NEES), an Energy Frontier Research Center funded by the U.S. Department of Energy, Office of Science, Basic Energy Sciences under Award number DESC0001160.

Appendix A. Supporting information

Supplementary data associated with this article can be found in the online version at doi:10.1016/j.nanoen.2017.06.014.

References

[1] N. Yabuuchi, M. Kajiyama, J. Iwatate, H. Nishikawa, S. Hitomi, R. Okuyama, R. Usui, Y. Yamada, S. Komaba, Nat Mater 11 (2012) 512–517.
[2] L. Mu, S. Xu, Y. Li, Y.-S. Hu, H. Li, L. Chen, X. Huang, Advanced Materials 27 (2015) 6928–6933.
[3] N. Yabuuchi, K. Kubota, M. Dahbi, S. Komaba, Chemical Reviews 114 (2014) 11636–11682.
[4] D.A. Stevens, J.R. Dahn, J Electrochem. Soc 147 (2000) 1271–1273.
[5] X. Xiang, K. Zhang, J. Chen, Advanced Materials 27 (2015) 5343–5364.
[6] W.-J. Li, S.-L. Chou, J.-Z. Wang, H.-K. Liu, S.-X. Dou, Nano Letters 13 (2013) 5480–5484.
[7] J. Qian, Y. Xiong, Y. Cao, X. Ai, H. Yang, Nano Letters 14 (2014) 1865–1869.
[8] C. Zhang, X. Wang, Q. Liang, X. Liu, Q. Weng, J. Liu, Y. Yang, Z. Dai, K. Ding, Y. Bando, J. Tang, D. Golberg, Nano Letters 16 (2016) 2054–2060.
[9] W. Li, S.-L. Chou, J.-Z. Wang, J.H. Kim, H.-K. Liu, S.-X. Dou, Advanced Materials 26 (2014) 4037–4042.
[10] Y. Kim, Y. Kim, A. Choi, S. Woo, D. Mok, N.-S. Choi, Y.S. Jung, J.H. Ryu, S.M. Oh, K.T. Lee, Advanced Materials 26 (2014) 4139–4144.
[11] Y. Zhu, Y. Wen, X. Fan, T. Gao, F. Han, C. Luo, S.-C. Liou, C. Wang, ACS Nano 9 (2015) 3254–3264.
[12] X. Fan, J. Mao, Y. Zhu, C. Luo, L. Suo, T. Gao, F. Han, S.-C. Liou, C. Wang, Advanced Energy Materials (2015). http://dx.doi.org/10.1002/aenm.201500174.
[13] J. Sun, H.-W. Lee, M. Pasta, Y. Sun, W. Liu, Y. Li, H.R. Lee, N. Liu, Y. Cui, Energy Storage Materials 4 (2016) 130–136.
[14] L. Ji, M. Gu, Y. Shao, X. Li, M.H. Engelhard, B.W. Arey, W. Wang, Z. Nie, J. Xiao, C. Wang, J.-G. Zhang, J. Liu, Advanced Materials 26 (2014) 2901–2908.
[15] W. Luo, F. Shen, C. Bommier, H. Zhu, X. Ji, L. Hu, Accounts of Chemical Research 49 (2016) 231–240.
[16] H. Kang, Y. Liu, K. Cao, Y. Zhao, L. Jiao, Y. Wang, H. Yuan, Journal of Materials Chemistry A 3 (2015) 17899–17913.
[17] Q. Li, Z. Li, Z. Zhang, C. Li, J. Ma, C. Wang, X. Ge, S. Dong, L. Yin, Advanced Energy Materials (2016). http://dx.doi.org/10.1002/aenm.201600376.
[18] J. Liu, P. Kopold, C. Wu, P.A. van Aken, J. Maier, Y. Yu, Energy & Environmental Science 8 (2015) 3531–3538.
[19] N. Liu, Z. Lu, J. Zhao, M.T. McDowell, H.-W. Lee, W. Zhao, Y. Cui, Nat Nano 9 (2014) 187–192.
[20] X. Fan, Y. Zhu, C. Luo, L. Suo, Y. Lin, T. Gao, K. Xu, C. Wang, ACS Nano 10 (2016) 5567–5577.
[21] J.-S. Bridel, S. Grugeon, S. Laruelle, J. Hassoun, P. Reale, B. Scrosati, J.-M. Tarascon, Journal of Power Sources 195 (2010) 2036–2043.
[22] L. Wu, X. Hu, J. Qian, F. Pei, F. Wu, R. Mao, X. Ai, H. Yang, Y. Cao, Energy & Environmental Science 7 (2014) 323–328.
[23] Y. Zhu, X. Han, Y. Xu, Y. Liu, S. Zheng, K. Xu, L. Hu, C. Wang, ACS Nano 7 (2013) 6378–6386.
[24] L. Liang, Y. Xu, C. Wang, L. Wen, Y. Fang, Y. Mi, M. Zhou, H. Zhao, Y. Lei, Energy & Environmental Science 8 (2015) 2954–2962.
[25] S. Qiu, X. Wu, L. Xiao, X. Ai, H. Yang, Y. Cao, Acs Appl Mater Interfaces 8 (2016) 1337–1343.
[26] K. Li, D. Su, H. Liu, G. Wang, Electrochim Acta 177 (2015) 304–309.
[27] L. David, R. Bhandavat, G. Singh, ACS Nano 8 (2014) 1759–1770.
[28] Y. Liu, N. Zhang, L. Jiao, Z. Tao, J. Chen, Advanced Functional Materials 25 (2015) 214–220.
[29] D.-H. Nam, T.-H. Kim, K.-S. Hong, H.-S. Kwon, ACS Nano 8 (2014) 11824–11835.
[30] L. Xiao, Y. Cao, J. Xiao, W. Wang, L. Kovarik, Z. Nie, J. Liu, Chemical Communications 48 (2012) 3321–3323.
[31] Y.-M. Lin, P.R. Abel, A. Gupta, J.B. Goodenough, A. Heller, C.B. Mullins, Acs Appl Mater Interfaces 5 (2013) 8273–8277.
[32] M.N. Tahir, B. Oschmann, D. Buchholz, X. Dou, I. Lieberwirth, M. Panthöfer, W. Tremel, R. Zentel, S. Passerini, Advanced Energy Materials 6 (2016). http://dx.doi.org/10.1002/aenm.201501489.
[33] H. Liu, M. Jia, Q. Zhu, B. Cao, R. Chen, Y. Wang, F. Wu, B. Xu, Acs Appl Mater Interfaces 8 (2016) 26878–26885.
[34] X. Wang, D. Chen, Z. Yang, X. Zhang, C. Wang, J. Chen, X. Zhang, M. Xue, Advanced Materials 28 (2016) 8645–8650.
[35] Z. Jian, W. Han, X. Lu, H. Yang, Y.-S. Hu, J. Zhou, Z. Zhou, J. Li, W. Chen, D. Chen, L. Chen, Advanced Energy Materials 3 (2013) 156–160.

Dr. Xiulin Fan received his bachelor degree and Ph.D. degree both in Materials Science and Engineering from Zhejiang University. From Feb. 2014 to Mar. 2017, he worked in University of Maryland-College Park as a post-doctoral research associate. He is currently an assistant research scientist at University of Maryland-College Park. His research interests are novel materials and their application in energy storage and conversion devices including lithium-ion batteries, sodium-ion batteries and hydrogen storage. He has more than 80 peer-reviewed journal publications.

Dr. Tao Gao received his bachelor degree in Automotive Engineering and M.S. degree in Mechanical Engineering both from Tsinghua University, and Ph.D. degree in Chemical Engineering from University of Maryland. His research interest is chemistry and system innovation for next generation batteries and electrochemical methods.

Dr. Chao Luo is currently a Postdoctoral Research Associate in Department of Chemical and Biomolecular Engineering, University of Maryland, College Park. He received his Bachelor's Degree in College of Chemistry and Molecular Sciences from Wuhan University in 2008, and then he got his Master's Degree with Professor Xuesong Wang in Technical Institute of Physics and Chemistry, Chinese Academy of Sciences in 2011. Afterwards, he obtained his Ph.D. with Prof. Chunsheng Wang in Department of Chemical and Biomolecular Engineering, University of Maryland, College Park. He is mainly interested in organic electrode materials and lithium sulfur batteries.

Dr. Fei Wang received his B.S. and Ph.D. in Physical Chemistry from Fudan University in 2015. He is currently a co-advised postdoctoral Research Associate in U.S.Army Research Lab and University of Maryland, College Park, USA. His research interests focus on energy storage devices including electrode materials, electrolyte, electrochemistry for rechargeable batteries and aqueous batteries.

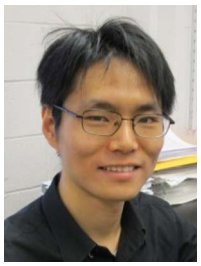

Dr. Junkai Hu is a Post-Doctoral Associate at the University of Maryland, College Park. He graduated with BS (2006) and MS (2009) degrees in Chemistry from Fudan University, Shanghai, China, and obtained his Ph.D. degree in Chemistry at the University of Maryland, College Park in 2015. His research interests include the synthesis of heterogeneous mesoporous materials for electrochemical energy storage devices and hazard gas adsorption/decomposition.

Prof. Chunsheng Wang is a full professor at University of Maryland College Park (UMCP). He was educated in materials science and trained in electrochemistry, and got his Ph.D. degree from Zhejiang University. He has more than 150 peer-reviewed journal publications and more than 25 years of experience in battery research. His Li-ion battery research has been highlighted in EFRC news by DoE in 2012, and by Chemical & Engineering News in 2013. He is a recipient of the University of Maryland Outstanding junior Researcher Award.